Available online at www.sciencedirect.com
ScienceDirect
International Journal of Solids and Structures 44 (2007) 6173–6186
INTERNATIONAL JOURNAL OF SOLIDS AND STRUCTURES
www.elsevier.com/locate/ijsolstr

Planar elastica inside a curved tube with clearance

Jen-San Chen *, Chia-Wei Li

Department of Mechanical Engineering, National Taiwan University, Taipei 10617, Taiwan

Received 26 December 2006; received in revised form 6 February 2007
Available online 13 February 2007

Abstract

In this paper, we study the planar deformation of a thin elastic wire inside a tubular housing with clearance. The center line of the tube is assumed to be in the shape of a planar circular arc. The wire is under longitudinal compression at the ends. This mechanics problem can be found in the stent deployment procedure commonly adopted in treating patients with coronary artery diseases. The tube and the wire are meant to model the patient's artery and the thin guidewire used in endovascular surgery, respectively. When the leading end of the guidewire encounters a blockage in the artery, the total length of the guidewire inside the artery varies as the wire undergoes bending deformation through the pushing at the other end. As a consequence, the leading end of the guidewire may not move forward the same distance that it is pushed in by the surgeon from the input end. It is also found that there exists a range of pushing force magnitude, in which one force magnitude may correspond to three different deformation patterns. Therefore, a deformation pattern jump may occur simply by adjusting the direction of the input force while holding the magnitude of the force constant. All these mechanics problems add more challenges to the surgeon's delicate tasks in performing the surgery effectively.

Keywords: Planar elastica; Curved tube with clearance; Stent procedure

1. Introduction

Stent procedures are commonly adopted in treating patients with coronary artery diseases (Schneider, 2003). The purpose of the surgery is to prop open the blocked artery with an inflatable balloon and place a stent in the lesion to help repave the artery wall. This is a desirable alternative to open-heart surgery for some patients. Stent procedures take place in a cardiac catheterization laboratory. During the surgery, the surgeon inserts a guidewire into the artery of the patient through a puncture in the groin. With the help of a fluoroscopic imaging system, the guidewire is first pushed into the neighborhood where artery repair is needed, as shown in Fig. 1(a). The next task is to pass the leading end of the guidewire through the narrow passageway of the lesion, as shown in Fig. 1(b). Depending on the complexity of the blockage, it may take the surgeon considerable efforts to accomplish the task. After the guidewire traverses the lesion successfully, a catheter

* Corresponding author. Tel.: +88 6 2 23661734; fax: +88 6 2 2 2363 1755.
E-mail address: jschen@ccms.ntu.edu.tw (J.-S. Chen).

0020-7683/$ - see front matter © 2007 Elsevier Inc. All rights reserved.
doi:10.1016/j.ijsolstr.2007.02.021

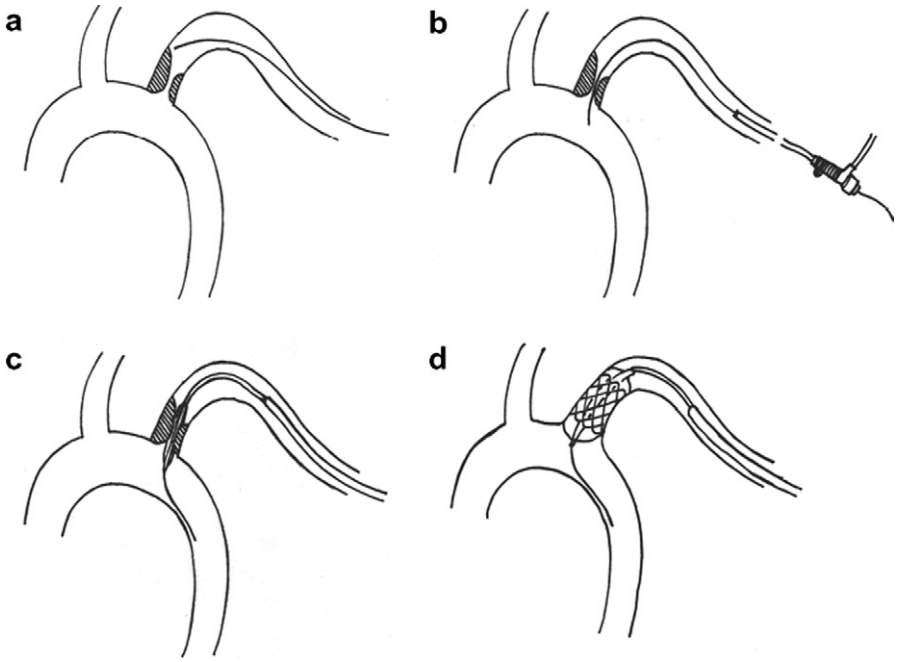

Fig. 1. Placement of a stent. (a) The guidewire is pushed near the place where artery repair is needed. (b) The guidewire traverses the lesion. (c) A catheter carrying an inflatable balloon with pre-mounted stent slides over the guidewire and passes through the lesion. (d) The balloon is inflated and the stent is deployed.

carrying an angioplasty balloon with pre-mounted stent may be slid over the guidewire and passed through the lesion, as shown in Fig. 1(c). Once the balloon is inflated and the stent deployed, as shown in Fig. 1(d), the balloon can then be deflated and withdrawn together with the guidewire, leaving the expanded stent in place to form a scaffold. This holds the artery open and improves blood flow to the heart muscle.

The length of the guidewire from the input end to the leading end is about 1 m. The diameter of the thinnest guidewire is 0.4 mm while the average diameter of human artery is in the order of 4 mm. The guidewire is manufactured in such a manner that it remains perfectly elastic following large deformation. As a consequence, the leading end near the lesion will not follow exactly the surgeon's hand movement at the input end, especially when the leading end encounters a blockage. For instance, it is common that the leading end will not move at all until the input end pushes in or pulls out more than 1 mm. Sometimes this movement lagging between the leading end and the surgeon's hand movement creates a problem when the opening of the lesion is small. A skilled surgeon needs a lot of training to get a grip of the feeling of this lagging phenomenon in the longitudinal motion of the wire. Recently there is a call from the circle of cardio-vascular surgeons to develop a tele-surgery technique, which can greatly reduce the surgeon's risk for long period of radioactive exposure by eliminating the need for the surgeon to stay in the same room with the patient. However, the inability of the leading end to match the input end movement precisely as described above presents a challenging task for control engineers to design such a medical robot. To overcome this obstacle, a thorough understanding of the mechanics involved in the stent procedure is desirable. This paper is a response to this need.

The unique mechanics problems mentioned above is apparently due to the clearance between the thin guidewire and the artery housing. This clearance provides the wire some room to bend when the wire is subjected to longitudinal push at the ends. The wire deformation studied in this paper is large and the subject may be considered as an elastica problem (Love, 1944; Timoshenko and Gere, 1961), a classical subject initiated by Euler and Lagrange over two centuries ago. Recently the interest in elastica has been rekindled due to many new applications, such as in electronic circuit strip wiring in lap-top computers (Plaut et al., 1999, 2004), compliant mechanism in MEMS design (Kimball and Tsai, 2002; Venanzi et al., 2005), and the packing arrangement of DNA within bacteriophage virus heads (Thompson and Champneys, 1996; Leung et al., 2005), to

name a few. These advances in elastica research focused on the deformation of a long elastic wire subjected to end loads, with no external constraints on the main body of the wire.

In other applications the bending deformation of the elastic wire may be restrained by certain lateral constraints. In the case when the elastic wire is fully restrained (without clearance) in a tubular housing with the shape of a circular arc and is under uniform rotation at one end, Panovko and Gubanova (1965) reported that the output end can undergo non-uniform rotation. Wires of this type can be found in the drives of vibrator instruments and in the brake line of bicycles. In the case when the elastic bar is constrained inside a straight channel with clearance, Domokos et al. (1997) and Holmes et al. (1999) investigated the planar buckling patterns and the bifurcation structure when the hinged-hinged bar is under prescribed end displacement. Their works were motivated by a need to understand the buckling behavior of polypropylene fibers in a 'stuffer box' manufacturing environment for non-woven fabrics. Chai (2002, 2006) carried out a combined experimental/analytical work to elucidate the energy absorption potential of laterally confined bars under monotonically increasing edge displacement. Roman and Pocheau (2002) used an elastica model to investigate the post-buckling response of bilaterally constrained thin plates subjected to a height reduction. The uniqueness of solutions for constrained elastica was addressed by Pocheau and Roman (2004).

In the drilling industry, engineers are interested in the buckling of a tube in an inclined wellbore under the action of its own weight and a compressive force at its upper end. The deformation of the constrained tube may be planar (Paslay and Bogy, 1964) or helical (Huang and Pattillo, 2000). In the case when the wellbore is curved, Wu and Juvkam-Wold (1995) studied the buckling and lockup of the tubes under compressive end force. Kuru et al. (2000) experimentally studied the buckling behavior of pipes and its influence on the axial force transfer in directional wells. The recent development in the research on the buckling of tubes inside wellbores can be found in a review paper by Cunha (2004). In spite of the extensive research on the subject of a constrained elastica discussed above, the deformation of an elastic wire inside a curved tubular housing, such as the one encountered in the stent deployment procedure, has not been attempted before.

2. Wire deformation when span angle ψ is small

First of all we assume that the elastic wire is inextensible and is stress-free when it is straight, and is uniform in all mechanical properties along its length. The cross section of the rigid tube is of annular shape. It is assumed that the diameter of the elastic wire is much smaller than the inner diameter of the cross section of the tube. In other words, there exists plenty of clearance between the wire and the tubular housing. It is assumed that the center line of the tube is in the shape of a plane circular curve.

Fig. 2 shows the plane section passing through the circular center line of the rigid tube. On this plane section the outer and inner radii of the tubular housing measured from the center of the curvature are r_o and r_i, respectively. ψ is the span angle of the tube. It is assumed that the deformed wire lies on this plane section.

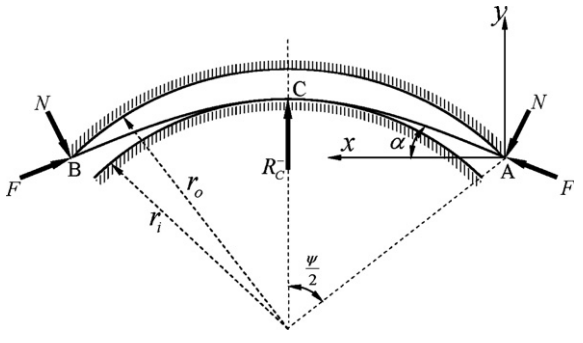

Fig. 2. Deformation pattern 1. The deformed wire is in point contact with the inner radius of the tube at the middle point *C*.

2.1. Deformation pattern 1: Point contact on inner radius at the middle point

The shape of the deformed wire depends on the span angle ψ. In the case when ψ is not very large, for instance, $\psi = \pi/2$ as shown in Fig. 2, the wire may contact the tube at three points, A, B, and C, when it is placed inside the tube. It is to be understood that the wire is longer than the tube at the input end A as depicted in lab demonstrations shown in Figs. 7 and 12, which will be discussed later. In Fig. 2 we only show the portion of the wire inside the tube. In this paper, we assume that the contact between the wire and the tube is frictionless. During the stent procedure the surgeon pushes in the wire from the input end. At the output end B the wire can be blocked by obstacles in the blood vessel. As a consequence, the wire can be considered as being under external compressive force F tangential to the wire at end points A and B. It is noted that the direction of the tangential force F changes with the deformation of the wire. Therefore, F is a non-conservative force. When F increases to a certain value, the wire and the inner radius may lose contact and eventually the wire will contact the outer radius instead. We will discuss these deformation patterns in due time. For the time being we focus on the deformation pattern described in Fig. 2 and explain how to determine the shape of the deformed wire.

First of all we establish an xy-coordinate system with the origin at point A. The moment equation at any point (x,y) of the deformed wire can be written as

$$\mathrm{EI}\frac{\mathrm{d}\theta}{\mathrm{d}s} = (-N\sin\alpha - F\cos\alpha)y + (-N\cos\alpha + F\sin\alpha)x \tag{1}$$

N is the force provided by the corner of the tube in the direction normal to the wire at point A. It is noted that the resultant force on the wire at point A is not constrained to be tangential to the wall or tangential to the wire. Furthermore, the bending moment in the wire at point A is assumed to be zero. α and θ are the slopes of the wire at point A and at the point (x,y), respectively. EI is the flexural rigidity of the wire. s is the length of the wire measured from point A. For convenience we introduce the following dimensionless parameters (with asterisks):

$$(s^*, x^*, y^*) = \frac{(s,x,y)}{r_o}, \qquad (N^*, F^*) = \frac{r_o^2}{\mathrm{EI}}(N,F) \tag{2}$$

Eqs. (2) represent the non-dimensionalization schemes for all lengths and forces in this paper. Similarly, we may introduce the dimensionless distributed force (per unit length) q^* and bending moment M^*, which will be used later, as

$$q^* = \frac{r_o^3}{\mathrm{EI}}q, \qquad M^* = \frac{r_o}{\mathrm{EI}}M$$

After substituting the above relations into Eq. (1), and dropping all the superposed asterisks thereafter for simplicity, we obtain the dimensionless equilibrium equation

$$\frac{\mathrm{d}\theta}{\mathrm{d}s} = (-N\sin\alpha - F\cos\alpha)y + (-N\cos\alpha + F\sin\alpha)x \tag{3}$$

After differentiating Eq. (3) with respect to s and noting the relations $\frac{\mathrm{d}y}{\mathrm{d}s} = \sin\theta$ and $\frac{\mathrm{d}x}{\mathrm{d}s} = \cos\theta$, we obtain

$$\frac{\mathrm{d}^2\theta}{\mathrm{d}s^2} = (-N\sin\alpha - F\cos\alpha)\sin\theta + (-N\cos\alpha + F\sin\alpha)\cos\theta \tag{4}$$

we multiply Eq. (4) by $\mathrm{d}\theta$ and integrate to obtain

$$\frac{1}{2}\left(\frac{\mathrm{d}\theta}{\mathrm{d}s}\right)^2 = N\sin(\alpha-\theta) + F\cos(\alpha-\theta) + D \tag{5}$$

D is an integration constant. From the boundary condition that curvature of the wire vanishes at point A, i.e.

$$\frac{\mathrm{d}\theta}{\mathrm{d}s} = 0 \quad \text{when } \theta = \alpha \tag{6}$$

we can determine that the integration constant $D = -F$. From Eq. (5) and Fig. 2 we can write

$$\mathrm{d}s = -\frac{\mathrm{d}\theta}{\sqrt{2N\sin(\alpha-\theta)+2F[\cos(\alpha-\theta)-1]}} \tag{7}$$

From Eq. (7) we can obtain

$$\mathrm{d}y = -\frac{\sin\theta\ \mathrm{d}\theta}{\sqrt{2N\sin(\alpha-\theta)+2F[\cos(\alpha-\theta)-1]}} \tag{8}$$

After integrating Eq. (8) from $\theta = \alpha$ to 0, we obtain the y-coordinate of point C as

$$\eta - \cos\frac{\psi}{2} = \int_0^\alpha \frac{\sin\theta\ \mathrm{d}\theta}{\sqrt{2N\sin(\alpha-\theta)+2F[\cos(\alpha-\theta)-1]}} \tag{9}$$

where η is defined as the radius ratio r_i/r_o. Similarly, the x-coordinate of point C can be calculated as

$$\sin\frac{\psi}{2} = \int_0^\alpha \frac{\cos\theta\ \mathrm{d}\theta}{\sqrt{2N\sin(\alpha-\theta)+2F[\cos(\alpha-\theta)-1]}} \tag{10}$$

For the problem at hand, geometric parameters η and ψ, as well as the external compression F, are specified. Eqs. (9) and (10) can then be used to determine the normal force N and slope α at point A. After determining N and α, the shape of the wire can be obtained by calculating the (x,y) coordinates of the deformed wire as

$$x = \int_\theta^\alpha \frac{\cos\phi\ \mathrm{d}\phi}{\sqrt{2N\sin(\alpha-\phi)+2F[\cos(\alpha-\phi)-1]}} \tag{11}$$

$$y = \int_\theta^\alpha \frac{\sin\phi\ \mathrm{d}\phi}{\sqrt{2N\sin(\alpha-\phi)+2F[\cos(\alpha-\phi)-1]}} \tag{12}$$

It is interesting to note that in the case when $F = 0$, the shape of the deformed wire is independent of the flexural rigidity EI. After determining the shape, the dimensionless total length l of the deformed wire inside the tube from point A to B can be calculated as

$$l = \int \mathrm{d}s = 2\int_0^\alpha \frac{\mathrm{d}\theta}{\sqrt{2N\sin(\alpha-\theta)+2F[\cos(\alpha-\theta)-1]}} \tag{13}$$

The dimensionless contact force R_C^- at the middle point can be determined from the relation

$$R_C^- = 2N\cos\alpha - 2F\sin\alpha \tag{14}$$

The superscript "−" signifies that the point contact occurs on the inner radius. Generally speaking, the contact force R_C^- decreases as the compressive force F increases. When F increases to a certain value such that R_C^- vanishes, the deformation pattern described in Fig. 2 ceases to be valid.

The question may arise as to whether it is possible for the wire to be in contact with the inner radius over a finite angular section, instead of point contact at the middle point as described in Fig. 2. This possibility can be ruled out by the following reasoning. If the wire is in contact with the inner radius over a finite angular section, the bending moment of the wire in the contact section is constant because the radius of curvature of the deformed wire is constant. As a result the shear force in the contact section is zero. The distributed force exerted by the inner radius on the wire can be balanced by the longitudinal force only when the longitudinal force is tensile. From the direction of the normal force N at the end points, we note that the longitudinal force must be in compression. Therefore, we conclude that the wire cannot contact the inner radius over a finite angular section.

It is noted that the wire deformation described in Fig. 2 can occur only when the span angle $\psi/2 > \psi_1 = \cos^{-1}\eta$. In the case when $\psi/2$ is smaller than ψ_1, the wire can remain straight inside the circular tube without deformation.

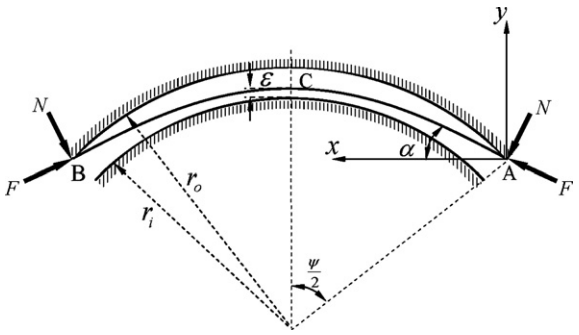

Fig. 3. Deformation pattern 2. The middle point of the deformed wire is elevated from the inner radius a small distance ε.

2.2. Deformation pattern 2: Elevated middle point

When F increases to a certain value, it is possible that the middle point of the wire in Fig. 2 will lose contact with the inner radius. As a consequence, the middle point C of the wire is elevated a small dimensionless distance ε, where $0 < \varepsilon < 1 - \eta$, as shown in Fig. 3. Due to symmetry, both the slope and the shear force at point C are zero. As a consequence, the normal force N is related to F by the equation

$$N = F \tan \alpha \tag{15}$$

Following a similar procedure as described in Fig. 2, α can be determined by solving the following equation:

$$\sin \frac{\psi}{2} = \frac{1}{\sqrt{2F}} \int_0^{\alpha} \frac{\cos\theta \, \mathrm{d}\theta}{\sqrt{\tan\alpha \sin(\alpha - \theta) + [\cos(\alpha - \theta) - 1]}} \tag{16}$$

After determining α from Eq. (16), the reactive force N can be determined from Eq. (15). The shape of the deformed wire can then be determined from Eqs. (11) and (12). When we assign the lower limit of the integration in Eq. (12) to zero, we should obtain the y coordinate of the middle point C, i.e.

$$\eta - \cos \frac{\psi}{2} + \varepsilon = \int_0^{\alpha} \frac{\sin\theta \, \mathrm{d}\theta}{\sqrt{2F}\sqrt{\tan\alpha \sin(\alpha - \theta) + [\cos(\alpha - \theta) - 1]}} \tag{17}$$

From Eq. (17) we can determine the elevation ε at the middle point. The total length l can then be determined from Eq. (13).

2.3. Deformation pattern 3: Point contact on the outer radius at middle point

After the elevation ε at the middle point as described above reaches $1 - \eta$, the wire deformation evolves to a new pattern in which the wire touches the outer radius at the middle point, as shown in Fig. 4. At the middle

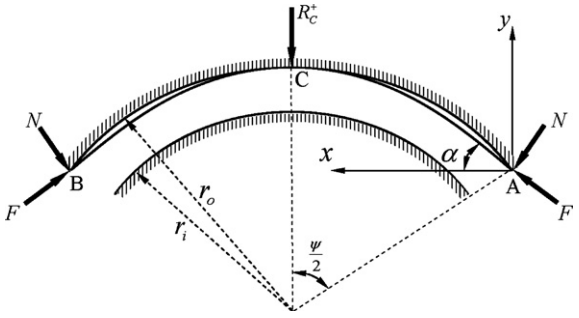

Fig. 4. Deformation pattern 3. The deformed wire is in point contact with the outer radius at the middle point C.

point C the wire is subjected to a point force R_C^+. The superscript "+" signifies that the point contact occurs on the outer radius. For this deformation pattern the N and α can be determined from Eqs. (9) and (10), except that the parameter η in Eq. (9) should be replaced by 1. After solving for N and α, the point contact force R_C^+ can be determined from the relation

$$R_C^+ = -2N\cos\alpha + 2F\sin\alpha \tag{18}$$

2.4. Deformation pattern 4: Distributed contact on the outer radius

The curvature at the middle point of the deformation pattern 3 decreases as the force F increases. After F increases to a certain value, the curvature at the middle point will reduce to 1. When the force F continues to increase beyond this point, the deformation pattern 3 will cease to be valid and the wire deformation evolves to a new pattern in which the wire touches the outer radius over an angular section ψ_H^+, as shown in Fig. 5. Between points H and A the wire is not in contact with the outer radius. In the contact region the wire is subjected to distributed load q. At point H the wire is subjected to an additional concentrated force R_H^+ from the outer radius of the tube. The problem now is to determine the angle ψ_H^+.

Similar to the formulation in deformation pattern 1, from the x and y coordinates of point H we obtain the following two equations:

$$\sin\frac{\psi}{2} - \sin\frac{\psi_H^+}{2} = \int_{\psi_H^+/2}^{\alpha} \frac{\cos\theta\ \mathrm{d}\theta}{\sqrt{2N\sin(\alpha-\theta) + 2F[\cos(\alpha-\theta)-1]}} \tag{19}$$

$$\cos\frac{\psi_H^+}{2} - \cos\frac{\psi}{2} = \int_{\psi_H^+/2}^{\alpha} \frac{\sin\theta\ \mathrm{d}\theta}{\sqrt{2N\sin(\alpha-\theta) + 2F[\cos(\alpha-\theta)-1]}} \tag{20}$$

One additional geometric constraint needed in calculating the angle ψ_H^+ is that the curvature of the deformed wire must be equal to 1 at point H, i.e.

$$2N\sin\left(\alpha - \frac{\psi_H^+}{2}\right) + 2F\left[\cos\left(\alpha - \frac{\psi_H^+}{2}\right) - 1\right] = 1 \tag{21}$$

After using Eq. (21) to replace the parameter N by F, the two unknowns ψ_H^+ and α can be determined from the two Eqs. (19) and (20). After determining ψ_H^+ and α, the normal force N can be determined from Eq. (21). It is noted that the radius of curvature of the wire in the contact region is a constant. As a result the dimensionless bending moment $M = 1$. From the force balance of a free body of the wire in the contact region we can conclude that the shear force is zero, and the dimensionless longitudinal compression P (tangential to the wire) and the distributive contact force q are constants and can be calculated as

$$q = P = N\sin\left(\alpha - \frac{\psi_H^+}{2}\right) + F\cos\left(\alpha - \frac{\psi_H^+}{2}\right) \tag{22}$$

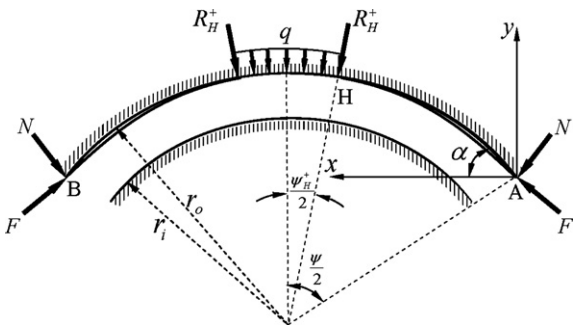

Fig. 5. Deformation pattern 4. The deformed wire is in contact with the outer radius over a finite angular section ψ_H^+.

Fig. 6 shows the effect of the magnitude of the compressive force F on the deformation of the wire when $\eta = 0.9$ and $\psi = \pi/2$. In Fig. 6(a) we show the evolution of the elevation ε at the middle point. When F increases from 0 to 4.2 the wire deforms according to the deformation pattern 1, i.e., the wire is in point contact with the inner radius at the middle point so that ε remains zero. In this deformation pattern the point contact force R_C^- decreases while the reactive normal force N increases, as shown in Figs. 6(b) and (c). The slope α at the end point continues to increase, as shown in Fig. 6(d). For clarity the start and the end of each deformation pattern are denoted by black dots, with the number of deformation pattern signified in Fig. 6(a). To achieve the deformation pattern 2, the magnitude of the force F has to decrease, while N and α at the end points continue to increase until F decreases to 3.5. In the meantime ε increases from 0 to 0.1. As F starts to increase from 3.5 from this point the wire deformation evolves to pattern 3, in which the wire contacts the outer radius at the middle point. The point contact force R_C^+ starts to increase from 0, as shown in Fig. 6(b). After F reaches 6.3, the curvature at the middle point decreases to 1 and the wire deformation evolves to pattern 4. The point force R_C^+ at point C splits into two point forces R_H^+ at H and continues to increase as F increases, as shown in Fig. 6(b). In this deformation pattern the contact angle ψ_H^+ increases from zero when F increases from 6.3, as shown in Fig. 6(d). The contact angle ψ_H^+ is equal to about $\pi/16$ when $F = 10$. In the meantime the distributed contact force q increases as F increases, as shown in Fig. 6(e). It is noted that ψ_H^+ will not be equal to ψ no matter how large the magnitude of F is. This is because the bending moments at the end points are zero, and as a consequence the curvature of the deformed wire will never match the curvature of the outer radius near the end points. In the deformation patterns 3 and 4 the middle point of the wire remains on the outer radius so that $\varepsilon = 0.1$ as shown in Fig.6(a).

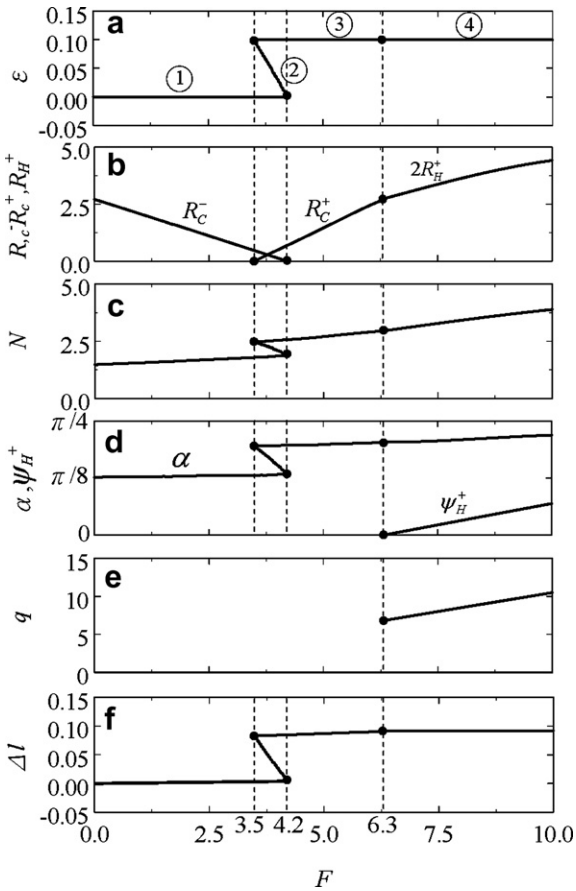

Fig. 6. Deformation evolution as the compressive force F increases for $\psi = \pi/2$ and $\eta = 0.9$. (a) Elevation ε at the middle point. (b) Point forces R_C^-, R_C^+, and $2R_H^+$. (c) Reactive force N. (d) Slope α at the end points and contact angle ψ_H^+. (e) Distributed contact force q. (f) Motion lagging Δl.

The total length of the wire inside the tube depends on the compressive force F and the deformation pattern. For instance, when the wire is first inserted into the tube, the total length inside the tube can be calculated from Eq. (13) with $F = 0$. We denote this length as l_0 . When F increases, the total length l inside the tube increases, as can also be calculated from Eq. (13). Therefore, if one end of the tube is blocked, we can push in the wire a distance $\Delta l = l - l_0$ from the other end with increasing F. This Δl is responsible for the lagging phenomenon we mentioned in the beginning of this paper. Fig. 6(f) shows Δl as a function of the compressive force F. It is noted that if the wire is undergoing deformation pattern 2 and the output end is blocked, then increasing the compressive force magnitude at the input end will result in the wire protruding out of the input end instead of pushing in.

It is interesting to note that for the force magnitude F between 3.5 and 4.2, there are three possible deformations (1, 2, and 3). Each deformation corresponds to a different direction α. In other words, there are three different forces in this range. Each of these three forces corresponds to a unique deformation. All these three deformation patterns are possible and can be realized in the laboratory. For a specified magnitude of the longitudinal force F, it is possible for the deformation to jump from pattern 1 to pattern 3 simply by adjusting the direction α at the ends.

To conveniently observe the wire deformation in the laboratory we build a circular channel with two walls on a table, as shown in Fig. 7. The span angle ψ is $\pi/2$. The outer and inner radii are 15 and 13.5 cm, respectively. Therefore, the radius ratio $\eta = 0.9$. The metallic wire is taken from a stent kit. The diameter of the wire is negligible compared to the clearance of the channel. The left end of the channel is blocked. The wire is pushed in by hand from the right-hand end. Fig. 7(a) shows the deformation (the black line) pattern 1 when the wire is initially put in the channel. The wire is in point contact with the inner radius at the middle point.

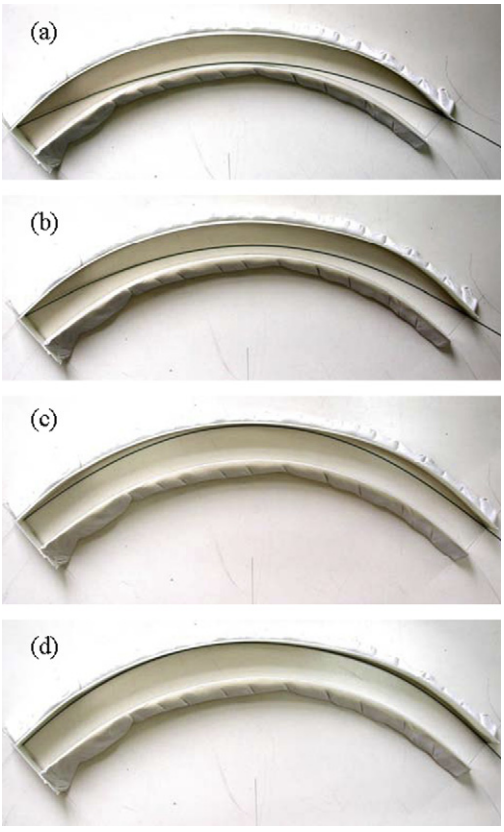

Fig. 7. Photograph of the wire deformation produced in the laboratory; $\psi = \pi/2$ and $\eta = 0.9$. (a) Deformation pattern 1, the wire is unloaded. (b) Deformation pattern 2. (c) Deformation pattern 3. (d) Deformation pattern 4.

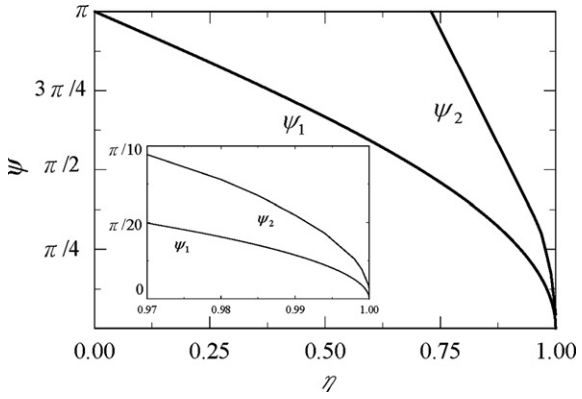

Fig. 8. Range of span angle $\psi_1 < \psi < \psi_2$ as a function of η, in which the deformation pattern 1 described in Fig. 2 is valid when $F = 0$. ψ_2 is the span angle when the curvature of the unloaded wire at point C is equal to $1/\eta$. The inset in the left-bottom corner shows the magnification of the range $0.97 < \eta < 1$.

Fig. 7(b),(c) and (d) show the deformation patterns 2, 3, and 4, respectively, when the wire is pushed in by hand.

3. Wire deformation when $\psi > \psi_2$

The deformation pattern 1 as described in Figs. 2 and 7(a) when the wire is not loaded by the compressive force F is no longer valid when the span angle ψ increases, say, to π. The problem lies in the fact that when ψ increases the deformed wire shape calculated in deformation pattern 1 may penetrate into the inner radius. This happens when the curvature of the deformed wire at the middle point C is larger than $1/\eta$. In Fig. 8 we show the range of the span angle $\psi_1 < \psi < \psi_2$ as a function of η, in which the deformation pattern 1 described in Fig. 2 is valid when $F = 0$. ψ_2 is the span angle when the curvature of the unloaded wire at point C is equal to $1/\eta$. For $\eta = 0.9$ ψ_2 is equal to 1.64. The inset in the left-bottom corner of Fig. 8 shows the magnification of the range $0.97 < \eta < 1$.

3.1. Deformation pattern 5: Four-point contact

Fig. 9 shows the correct deformation pattern when $\psi = \pi > \psi_2$ and F is small. The wire is in point contact with the inner radius at point H, which is located by the angle $\psi_H^-/2$ measured from the symmetric centerline. The wire is subjected to point force R_H^- at point H. At middle point C the wire is elevated by a small distance ε. From the force balance in the y direction, we can relate R_H^- to N and F by

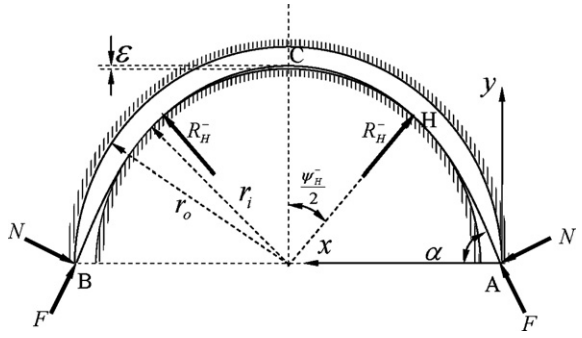

Fig. 9. Deformation pattern 5. The deformed wire is in point contact with the inner radius at angular position $\psi_H^-/2$.

$$R_H^- = \frac{N\cos\alpha - F\sin\alpha}{\cos\frac{\psi_H^-}{2}} \tag{23}$$

The deformation in the segment AH is similar to the one described in Fig. 2. Therefore, the coordinates (x_H, y_H) can be calculated from

$$\begin{aligned} x_H &= -\eta\sin\frac{\psi_H^-}{2} + \sin\frac{\psi}{2} \\ &= \int_{\psi_H^-/2}^{\alpha} \frac{\cos\theta\ \mathrm{d}\theta}{\sqrt{2N\sin(\alpha-\theta) + 2F[\cos(\alpha-\theta)-1]}} \end{aligned} \tag{24}$$

Similarly,

$$\begin{aligned} y_H &= \eta\cos\frac{\psi_H^-}{2} - \cos\frac{\psi}{2} \\ &= \int_{\psi_H^-/2}^{\alpha} \frac{\sin\theta\ \mathrm{d}\theta}{\sqrt{2N\sin(\alpha-\theta) + 2F[\cos(\alpha-\theta)-1]}} \end{aligned} \tag{25}$$

To calculate the deformation in the segment CH, we first draw the free body diagram of this segment and establish a local xy coordinate system with the origin at point H, as shown in Fig. 10. The shear force Q_H (normal to the wire), longitudinal force P_H (tangential to the wire), and bending moment M_H at point H can be obtained from the equilibrium condition in the segment AH as

$$Q_H = N\cos\left(\alpha - \frac{\psi_H^-}{2}\right) - F\sin\left(\alpha - \frac{\psi_H^-}{2}\right) \tag{26}$$

$$P_H = N\sin\left(\alpha - \frac{\psi_H^-}{2}\right) + F\cos\left(\alpha - \frac{\psi_H^-}{2}\right) \tag{27}$$

$$M_H = (-N\sin\alpha - F\cos\alpha)y_H + (-N\cos\alpha + F\sin\alpha)x_H \tag{28}$$

From Fig. 10, we can write the moment equation for the deformed wire as

$$\frac{\mathrm{d}\theta}{\mathrm{d}s} = (R_H^- - Q_H)x\cos\frac{\psi_H^-}{2} + (R_H^- - Q_H)y\sin\frac{\psi_H^-}{2} + P_H\left(x\sin\frac{\psi_H^-}{2} - y\cos\frac{\psi_H^-}{2}\right) + M_H \tag{29}$$

It is noted that the R_H^-, Q_H, P_H, and M_H in Eq. (29) can be related to N and F by Eqs. (23), (26), (27), and (28). Eq. (29) can be differentiated and simplified to the following equation:

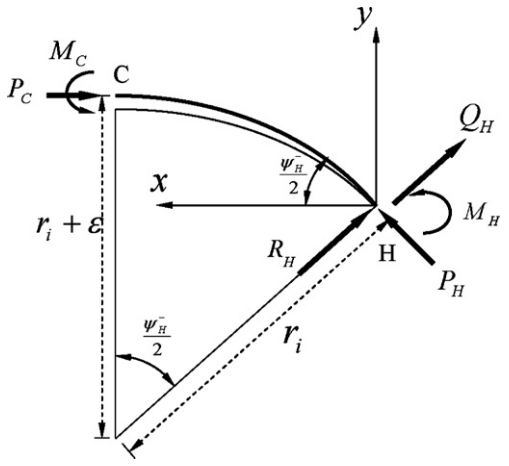

Fig. 10. Free body diagram of the segment CH for deformation pattern 5.

$$\frac{d^2\theta}{ds^2} = -N\cos(\alpha-\theta) + F\sin(\alpha-\theta) + R_H^-\cos\left(\frac{\psi_H^-}{2}-\theta\right) \tag{30}$$

We can now follow the formulation as described in deformation pattern 2 to obtain the following two equations

$$\eta\sin\frac{\psi_H^-}{2} = \int_0^{\psi_H^-/2}\frac{\cos\theta\ d\theta}{\sqrt{Z}} \tag{31}$$

$$\eta\left(1-\cos\frac{\psi_H^-}{2}\right)+\varepsilon = \int_0^{\psi_H^-/2}\frac{\sin\theta\ d\theta}{\sqrt{Z}} \tag{32}$$

where Z is defined as

$$\begin{aligned} Z = {} & -2\left(\frac{N\cos\alpha - F\sin\alpha}{\cos(\psi_H^-/2)}\right)\sin\left(\frac{\psi_H^-}{2}-\theta\right) + 2N\left[\sin(\alpha-\theta)-\sin\left(\alpha-\frac{\psi_H^-}{2}\right)\right] \\ & + 2F\left[\cos(\alpha-\theta)-\cos\left(\alpha-\frac{\psi_H^-}{2}\right)\right] \\ & + \left\{F\left[\cos\left(\frac{\psi}{2}\right)-\eta\cos\left(\alpha-\frac{\psi_H^-}{2}\right)\right] - N\left[\sin\left(\frac{\psi}{2}-\alpha\right)+\eta\sin\left(\alpha-\frac{\psi_H^-}{2}\right)\right]\right\}^2 \end{aligned} \tag{33}$$

We can now use the four Eqs. (24), (25), (31) and (32) to solve for the four unknowns N, α, ψ_H^-, and ε.

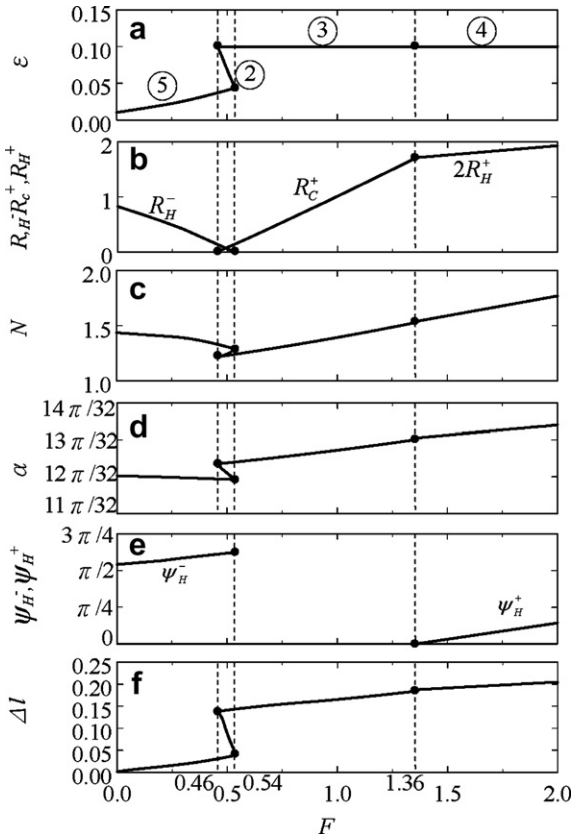

Fig. 11. Deformation evolution as the compressive force F increases for $\psi = \pi$ and $\eta = 0.9$. (a) Elevation ε at the middle point. (b) Point forces R_H^-, R_C^+, and $2R_H^+$. (c) Reactive normal force N. (d) Slope α at the end points. (e) Contact angles ψ_H^- and ψ_H^+. (f) Motion lagging Δl.

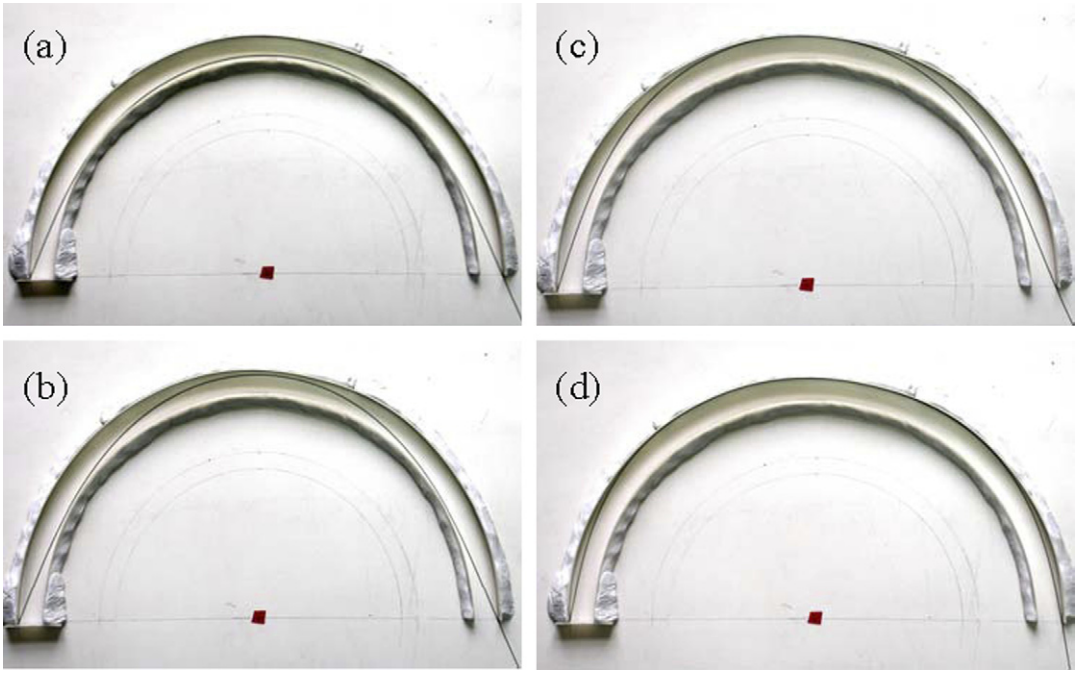

Fig. 12. Photograph of the wire deformation produced in the laboratory; $\psi = \pi$ and $\eta = 0.9$. (a) Deformation pattern 5, the wire is unloaded. (b) Deformation pattern 2. (c) Deformation pattern 3. (d) Deformation pattern 4.

Fig. 11 shows the deformation evolution when $\psi = \pi$ and $\eta = 0.9$. The main difference between Figs. 11 and 6 is the first part of the deformation. In Fig. 11 the wire is first in deformation pattern 5. For the unloaded wire (F=0), the middle point is floating with $\varepsilon = 0.01$ and the wire touches the inner radius at $\psi_H^-/2$=0.85. When F increases from 0 to 0.54, ε increases to 0.045. In the meantime both the reactive force N and the slope α decrease while the contact angle $\psi_H^-/2$ increases to 0.98, as shown in Figs. 11(c), (d), and (e). The middle point of the wire still floats in the air. However, the wire loses contact with the inner radius as the point force R_H^- vanishes, as shown in Fig. 11(b). From this point on the deformation pattern evolves to patterns 2, 3, and 4 similar to the situation in Fig. 6 for $\psi = \pi/2$.

Similar to Fig. 7 we also build a channel for the case of $\psi = \pi$ in Fig. 12. The outer and inner radii are 15 cm and 13.5 cm, respectively. Fig. 12 (a) shows the deformation pattern 5 when the wire is not loaded. Figs. 12(b), (c) and (d) show the deformation patterns 2, 3, and 4, respectively, when the wire is pushed in by hand. In Fig. 12(b) the wire is neither in contact with the inner radius nor with the outer radius except at the ends.

4. Conclusions

In this paper, we study the deformation of a thin elastic wire inside a tubular housing with clearance. The center line of the rigid tube is in the shape of a planar circular arc. The wire is under longitudinal compression at the ends. The deformation pattern of the wire depends on the span angle of the circular tube and the ratio between the inner and outer radii of the tube. This mechanics problem can be found in the stent procedure commonly adopted in treating patients with coronary artery diseases. The tube and the wire are meant to model the patient's artery and the thin guidewire used in endovascular surgery, respectively. In this paper, we present two cases for radius ratio 0.9, one with span angle $\pi/2$, and the other with span angle π. For these two different span angles the deformation patterns can be different. For radius ratio 0.9, it is relatively easy to observe these deformation patterns in the laboratory. Some conclusions can be summarized as follows:

(1) Due to the constraint on the inner and outer radii, the deformation pattern of the wire changes as the magnitude of the external compression at the end changes. For the two cases discussed in this paper, four different deformation patterns are associated with each case.
(2) The total length of the wire inside the tube varies as the wire undergoes bending deformation through the exertion of end compression. This mechanism is responsible for the lagging phenomenon observed in the laboratory. In other words, the leading end of the guidewire may not move forward the same distance that it is pushed in by the surgeon from the input end, especially when the leading end encounters obstacles.
(3) There exists a range of compressive force magnitude for which one force magnitude corresponds to three different deformation patterns. Each of these three deformation patterns corresponds to a different slope of the compressive force. All of them are realizable in the laboratory. As a consequence, a deformation pattern jump may occur simply by adjusting the direction of the input force while holding the magnitude of the force constant.

References

Chai, H., 2002. On the post-buckling behavior of bilaterally constrained plates. International Journal of Solids and Structures 39, 2911–2926.
Chai, H., 2006. On the crush worthiness of a laterally confined bar under axial compression. Journal of Applied Mechanics 73, 834–841.
Cunha, J.C., 2004. Buckling of tubulars inside wellbores: Review on recent theoretical and experimental works. SPE Drilling and Completion 19, 13–19.
Domokos, G., Holmes, P., Royce, B., 1997. Constrained Euler buckling. Journal of Nonlinear Science 7, 281–314.
Holmes, P., Domokos, G., Schmitt, J., Szeberenyi, I., 1999. Constrained Euler buckling: an interplay of computation and analysis. Computer Methods in Applied Mechanics and Engineering 170, 175–207.
Huang, N.C., Pattillo, P.D., 2000. Helical buckling of a tube in an inclined wellbore. International Journal of Non-Linear Mechanics 35, 911–923.
Kimball, C., Tsai, L.-W., 2002. Modeling of flexural beams subjected to arbitrary end loads. Journal of Mechanical Design 124, 223–235.
Kuru, E., Martinez, A., Miska, S., Qiu, W., 2000. The buckling behavior of pipes and its influence on the axial force transfer in directional wells. Journal of Energy Resources Technology 122, 129–135.
Leung, A.Y.T., Kunag, J.L., Lim, C.W., Zhu, B., 2005. Spatial chaos of buckled elastica by the Kirchhoff analogy of a gyrostat. Computers and Structures 83, 2395–2413.
Love, A.E., 1944. A Treatise on the Mathematical Theory of Elasticity. Dover Publications, New York.
Panovko, Y.G., Gubanova, I.I., 1965. Stability and Oscillations of Elastic Systems, Paradoxes, Fallacies, and New Concepts. Consultants Bureau Enterprises, Inc., New York.
Paslay, P.R., Bogy, D.B., 1964. The stability of a circular rod laterally constrained to be in contact with an inclined circular cylinder. Journal of Applied Mechanics 31, 605–610.
Plaut, R.H., Suherman, S., Dillard, D.A., Williams, B.E., Watson, L.T., 1999. Deflections and buckling of a bent elastica in contact with a flat surface. International Journal of Solids and Structures 36, 1209–1229.
Plaut, R.H., Taylor, R.P., Dillard, D.A., 2004. Postbuckling and vibration of a flexible strip clamped at its ends to a hinged substrate. International Journal of Solids and Structures 41, 859–870.
Pocheau, A., Roman, B., 2004. Uniqueness of solutions for constrained elastica. Physica D 192, 161–186.
Roman, B., Pocheau, A., 2002. Postbuckling of bilaterally constrained rectangular thin plates. Journal of the Mechanics and Physics of Solids 50, 2379–2401.
Schneider, P.A., 2003. Endovascular skills: guidewire and catheter skills for endovascular surgery. Marcel Dekker Inc., New York.
Thompson, J.M.T., Champneys, A.R., 1996. From helix to localized writhing in the torsional post-buckling of elastic rods. Proceedings of Royal Society of London A 452, 117–138.
Timoshenko, S.P., Gere, J.M., 1961. Theory of Elastic Stability. McGraw Hill, New York.
Venanzi, S., Giesen, P., Parenti-Castelli, V., 2005. A novel technique for position analysis of planar compliant mechanisms. Mechanism and Machine Theory 40, 1224–1239.
Wu, J., Juvkam-Wold, H.C., 1995. The effect of wellbore curvature on tubular buckling and lockup. Journal of Energy Resources Technology 117, 214–218.